Available online at www.sciencedirect.com
ScienceDirect
International Journal of Heat and Fluid Flow 28 (2007) 388–406
International Journal of HEAT AND FLUID FLOW
www.elsevier.com/locate/ijhff

Modelling the mean temperatures used for calculating heat and mass transfer in sprays

A.P. Watkins *

Energy, Environment and Climate Change Research Group, School of Mechanical, Aerospace and Civil Engineering, University of Manchester, Sackville Street, Manchester M60 1QD, UK

Received 22 March 2006; received in revised form 3 July 2006; accepted 29 July 2006
Available online 25 September 2006

Abstract

This paper deals with a variation on the approach to the modelling of sprays developed by Beck, J.C., Watkins, A.P., 2003a. On the development of a spray model based on drop-size moments. Proc. R. Soc. Lond. A 459 1365. In that model the size information concerning the spray is obtained by solving transport equations for two moments of the drop number size distribution, and their respective mean velocities, and obtaining two other moments from an assumed size distribution. The sub-models required for hydrodynamic phenomena, such as drop drag, break-up and collisions, have been presented in Beck, J.C., Watkins, A.P., 2002. On the development of spray sub-models based on droplet size moments. J. Comp. Phys. 182 586–621. The heat and mass transfer sub-models are described in Beck, J.C., Watkins, A.P., 2003b. The droplet number moments approach to spray modelling: the development of heat and mass transfer sub-models. Int. J. Heat and Fluid Flow 24 242–259. A single transport equation for the energy of the liquid phase is solved from which the local value of the volume-average liquid temperature is obtained. Consequently all the heat and mass transfer phenomena are related to this temperature. In practice it is the drop surface temperature that determines the heat and mass transfer rates. This paper explores the development and application of a simple model that assumes a parabolic temperature profile within individual drops to calculate a surface-area-average temperature for the spray locally. The models are applied to the simulation of sprays having assumed drop size distributions with Sauter mean radii at inlet in the 7–70 μm range. The use of surface-area-averaged temperatures, in place of volume-averaged ones, results in substantially higher levels of mass being evaporated from the drops. This is predominantly because of the increased film mean temperature and resulting increases in the vapour pressure in the film. The effects of the fuel used are also explored. The role of the vapour pressure in the film is again found to be the important parameter determining the different mass transfer rates for the different fuels. Comparisons made with spray penetration data of diesel fuel for a wide range of injector and ambient gas conditions indicate that the model reacts correctly to changes in these parameters. Comparisons are also made with measured liquid velocities and mean drop sizes. The importance of break-up and collision models on both the hydrodynamics and the heat and mass transfer in simulations made with the larger drops at inlet is demonstrated.

Keywords: Spray modelling; Drop number size moments; Heat and mass transfer

1. Introduction

For many years computational spray modelling has employed the particle-source-in-cell method (Crowe et al., 1977), or the Discrete Drop Model (DDM) (Ducowicz, 1980). These have been used successfully for a wide range of spray simulations, ranging from, for example, fuel sprays in engines (Gosman and Johns, 1980; Reitz, 1987; Chen and Perreira, 1992; Amsden et al., 1989), to medical applications (Dunbar et al., 1997) through to electrostatic agricultural sprays (Jahannama et al., 2005). The DDM involves solving the equations of motion for a turbulent carrier gas in an Eulerian scheme, and integrating Lagrangian equations of motion for liquid drops along true path

* Tel.: +44 161 306 3706; fax: +44 161 306 3723.
E-mail address: paul.watkins@manchester.ac.uk

0142-727X/$ - see front matter © 2006 Elsevier Inc. All rights reserved.
doi:10.1016/j.ijheatfluidflow.2006.07.007

Nomenclature

A	surface Area
a, b, c	constants in parabolic temperature equation, collision regimes
b	impact parameter
Bi	Biot number
B_M	mass transfer number
B_Q	source term due to break-up
c_p	specific heat capacity
c_μ, $c_{\varepsilon 1}$, $c_{\varepsilon 2}$, $c_{\varepsilon 3}$	turbulence parameters
D	mass diffusivity
E	total energy
Fo	Fourier number
f	vapour mass fraction
G	generation of turbulence kinetic energy
h	convective heat transfer coefficient
k	thermal conductivity
k	turbulent kinetic energy
L	latent heat of vaporisation
Le	Lewis number
M	molecular weight
N	number
$n(r)$	number distribution
Nu	Nusselt number
Pr	Prandtl number
P	pressure, probability
p	partial pressure
p_r	pressure ratio
Q_i	drop moment
$\dot{Q}$	heat transfer rate
R	gas constant
Re	Reynolds number
R_0	universal gas constant
r	radius, radial coordinate
S	source term
Sc	Schmidt number
Sh	Sherwood number
T	temperature
t	time
U	velocity
We	Weber number
x	Cartesian coordinate
z	axial coordinate

Greek symbols

α, β	coefficients in surface-area-averaged liquid temperature equation
δ_{ij}	Kronecker Delta
ε	turbulence kinetic energy dissipation rate
Γ	diffusivity
μ	dynamic viscosity
ν	kinematic viscosity
θ	void fraction
ρ	density
σ	turbulent Prandtl number, surface tension
χ	parameter in transport equations
φ	independent variable
ψ	damping coefficient

Subscripts

a	air
b	bag break-up
c	convective, drop centre
coal	coalescence
coll	collisions
d	drop
e	energy
eff	effective
g	gas
i	moment index
in	input to liquid, initial
j, k	direction index and velocity component
k	turbulence kinetic energy
l	liquid
lam	laminar
m	mass, film mean
q	moment
rel	relative
s	drop surface, stripping break-up
sep	separation
smaller	smaller drop
U	velocity
v	vapour
ε	dissipation rate
φ	independent variable
0	number-averaged
1	radius-averaged
2	surface-area-averaged
3	volume-averaged
32	sauter mean

Superscripts

$\bar{}$	volume-averaged
l	Liquid

lines. These two calculation schemes, and therefore the two phases, are then coupled through source terms in the transport equations.

The major disadvantage of the DDM is that it is not able to provide grid independent results (Abraham, 1997). This is because the liquid volume fraction in any computational cell cannot rise above about 10% without numerical instabilities occurring. Consequently, large cells are required around the nozzle of the injector. This has serious effects on the accuracy of the calculated liquid/gas mixing

there. Also, the stochastic models employed in producing the chaotic turbulent motion of sprays require a large number of drop parcels to produce a smooth representation of the spray and are therefore computationally expensive, although these are generally recognised to be more efficient in this regard than the multi-size range Eulerian alternatives that are available, e.g. Mostafa and Elghobashi (1985).

An alternative approach to the modelling of poly-disperse sprays has been extensively documented in the literature (Beck and Watkins, 2002, 2003a,b,c, 2004). The liquid and gas are both represented in the Eulerian formulation, and the full poly-disperse nature of the spray flow is captured whilst only considering the liquid as one phase. The first four moments of the drop size number distribution provide an adequate representation of the poly-disperse nature of the spray, and by solving equations for these parameters, a fully multi-size model of the spray has been constructed. The use of these moments means that the spray is dealt with in terms of average quantities, allowing a smooth representation of the drop size distribution at all points, rather than a discrete representation. This is an advantage even when considering phenomena such as drop break-up in which a discrete representation of the outcome of the break-up would seem most appropriate, for it is not the break-up process itself which is important but rather its effect on the overall size distribution of the spray. This latter quantity should remain smooth. The moments are also the terms needed in order to produce the source terms for the effects of the spray on the gas phase. Another feature of the model is the derivation of moment-averaged quantities. The role of moment-averaged velocity components has been emphasised in Beck and Watkins (2003a). These allow different parts of the spray to move at different velocities, depending on the local make up of the number size distribution and hence lead to a re-distribution of the drops depending on their sizes.

The major purpose of this paper is to consider and model the effects of moment-averaged temperatures. In the model to-date, only a single volume-averaged temperature has been considered for the spray locally (Beck and Watkins, 2003b). Most mass and heat transfer phenomena in sprays are surface-area related, rather than volume based. The objective here then is to develop a model for the surface-area-averaged temperature. The model employs an assumed temperature variation through a drop to derive a surface temperature. These surface temperatures are then averaged over the local spray number size distribution to obtain the averaged surface temperature for the spray locally. The relevant equations used in this model are derived in the next section, after the basic moment averaging approach has been outlined for clarity. The heat and mass transfer models are then presented in the context of this model. These equations Eqs. (5)–(27) form the new model that is unique to this research. Most of the other equations presented here give a précis of the Beck and Watkins model and have been presented in earlier publications. These are required for clarity. Model test cases are presented in the next section, along with comparison with two set of experimental data, including high temperature ambient gas cases, before conclusions are drawn in the final section of the paper.

2. Model formulation

2.1. Drop number size distribution moments

The moments of the drop number size distribution are defined by

$$Q_i = \int_0^\infty n(r_s) r_s^i \, \mathrm{d}r_s \tag{1}$$

where r_s is the radius of the drop surface and $n(r_s)$ is the number of drops having radii between limits $r_s + \mathrm{d}r_s/2$ and $r_s - \mathrm{d}r_s/2$.

In the model the first four moments, Q_0 to Q_3 are used. At a particular point in space and time, Q_0 is the total number of drops present, Q_1 is the total sum of radii of the drops, $4\pi Q_2$ is the total surface area of the drops and $4\pi Q_3/3$ is the total volume of the drops which, assuming that locally all drops to have the same liquid density, also defines the mass of liquid present per unit volume. This means that the transport equation for Q_3 is equivalent to a liquid phase continuity equation. It has been shown in earlier publications (Beck and Watkins, 2002, 2003a) that the modelling of important spray phenomena, such as the drag on the drops and the modelling of drop break-up, also require values for the other three moments.

2.2. Moment-average quantities

Previous publications of the model have also demonstrated that to write Eulerian transport equations for the drop moments, the mean speed at which the moments are convected has to be defined and that the mean speed must be different for each of the moments. Larger drops experience less drag and generally have higher velocities than the smaller drops. This effect is modelled by ensuring that the mass-average velocity is higher than the surface-area-average velocity. The jth moment-average liquid velocity component U_{lij} averaged over the ith moment Q_i is defined as

$$U_{lij} = \frac{\int_0^\infty U_{dj} n(r_s) r_s^i \, \mathrm{d}r_s}{Q_i} \tag{2}$$

The result of defining both the drop number moments and the moment-averaged velocities is that the former provide a representation of the distribution of drop sizes at each point in space and time, while the latter provide the means by which the distribution of drop size can change in space and time, along with sub-models for drop dynamic phenomena such as break-up and collisions (Beck and Watkins (2002)). These concepts allied together provide a picture of the behaviour of a poly-disperse spray.

2.3. Liquid phase transport equations

In the current version of the model, transport equations are solved for the Q_2 and Q_3 moments and their respective momentum equations. These can be collectively written as

$$\frac{\partial}{\partial t}(\chi\varphi) + \frac{\partial}{\partial x_k}(\chi U_{lik}\varphi) = \frac{\partial}{\partial x_k}\left(\Gamma_\varphi \frac{\partial \varphi}{\partial x_k}\right) - S_\varphi \tag{3}$$

The forms of parameters χ, Γ_φ and S_φ and subscript i are given in Table 1. In that table, the source term S_m is the mass evaporated from the liquid phase. The source term S_{Q2} expresses the change in the surface-area-averaged moment due to surface area changes brought about by drop collisions, drop break-up and evaporation. The term B_{Q2} is the component of S_{Q2} due to drop break-up. The source terms S_{Ul3i} and S_{Ul2i} represent the transfer of momentum from the liquid phase due primarily to drag, the former being transferred to the gas phase. The derivations of these source terms are discussed in detail in Beck and Watkins (2002). The term $\psi\nu_l$ is the liquid phase turbulent viscosity derived by Mostafa and Mongia (1987) as a damped form of the gaseous turbulence, where the damping is incorporated through the use of a drop Schmidt number and the coefficient ψ (Melville and Bray, 1979). In these calculations a value of 0.7 is used throughout for this coefficient.

Once values of Q_2 and Q_3 are known, the local Sauter mean radius (SMR) r_{32} is evaluated from Q_3/Q_2. An assumed size distribution function given by

$$\frac{\mathrm{d}n(r_s)}{\mathrm{d}r_s} = \frac{16 r_s}{r_{32}^2}\exp\left(-\frac{4r_s}{r_{32}}\right) \tag{4}$$

is then truncated at one end to fit the SMR. Values of Q_1 and Q_0 are then evaluated from the truncated distribution. Details of these processes are given in Beck and Watkins (2002, 2003a).

2.4. Liquid phase temperature equations

In Beck and Watkins (2003b) the conservation equation for liquid phase energy E_l is written in the same form as Eq. (3), with the parameters given in Table 1. The form of the source term S_E is derived in that publication, but is re-derived below for the new model presented here. This equation is for the transport of volume-averaged energy, which results in a volume-averaged temperature locally for the spray. The purpose of this section is to derive an additional equation for the local value of surface-area-averaged temperature.

Table 1
Forms of χ, i, Γ_φ and S_φ for liquid phase equations

φ	χ	i	Γ_φ	S_φ
Q_3	$\frac{4}{3}\pi\rho_l$	3	0	S_m
Q_2	1	2	0	S_{Q2}
U_{l3j}	$\frac{4}{3}\pi\rho_l Q_3$	3	$\frac{4}{3}\pi\rho_l Q_3\psi\nu_l$	$S_{Ul3j} + U_{l3j}S_m$
U_{l2j}	Q_2	2	$Q_2\psi\nu_l$	$S_{Ul2j} + U_{l3j}B_{Q2} + U_{l2j}(S_{Q2} - B_{Q2})$
E_l	$\frac{4}{3}\pi\rho_l Q_3$	3	$\frac{4}{3}\pi\rho_l Q_3\psi\nu_l$	$S_E + E_l S_m$

The first assumption made in this model is that all drops have a spherical shape; this is a fundamental assumption of the moments modelling approach. The second assumption is that a parabolic profile of temperature exists across any drop from the centre to the surface. The development of the theory of drop heating has been reviewed by Sirignano (1999). There are a number of models that have been proposed that allow the temperature profile to be calculated. However, many of these have been developed and used only for single drop studies and have not generally been adopted for computational fluid dynamics (CFD) modelling of sprays because of the complexity involved and the number of drops that have to be treated in a spray. Instead for the modelling of sprays an isothermal assumption is made for each drop, although the temperature of each drop may be different. Recently Dombrovsky and Sazhin (2003) showed that, for the very small spray drops employed in diesel engines, a parabolic temperature profile assumption gave results for the surface temperature and mean temperature of a single drop that were comparable in accuracy to those produced by more complicated models.

The assumed temperature profile within any given drop is thus

$$T(r) = a + br + cr^2 \tag{5}$$

The constants a and b are found from the boundary conditions, i.e. $T = T_s$ at $r = r_s$, where subscript 's' denotes the drop surface, and $\frac{\mathrm{d}T}{\mathrm{d}r} = 0$ at $r = 0$. Thus $b = 0$ and $a = T_s - cr_s^2$. The constant c is found from the definition of the drop volume-average temperature $\overline{T}_d$

$$\overline{T}_d \int_0^{r_s} r^2\,\mathrm{d}r = \int_0^{r_s} Tr^2\,\mathrm{d}r \tag{6}$$

Thus the form of the parabolic temperature profile expressed in terms of T_s and $\overline{T}_d$ is

$$T(r) = T_s - \frac{5}{2}(T_s - \overline{T}_d)\left[1 - \left(\frac{r}{r_s}\right)^2\right] \tag{7}$$

The heat transferred by conduction into the drop is evaluated at the drop surface

$$\dot{Q}_{in,d} = k_l A_s \left.\frac{\mathrm{d}T}{\mathrm{d}r}\right|_{r=r_s} = k_l 4\pi r_s^2 \frac{5(T_s - \overline{T}_d)}{r_s} = 20\pi k_l r_s (T_s - \overline{T}_d) \tag{8}$$

where k_l is the liquid thermal conductivity.

The total heat transfer rate into all the spray drops locally is evaluated by integration over all the drops in a control volume by means of the number size distribution, thus

$$\dot{Q}_{\text{in}} = \int_0^\infty \dot{Q}_{\text{in,d}} n(r_s)\,\mathrm{d}r_s = 20\pi k_l \int_0^\infty (T_s - \overline{T}_d) r_s n(r_s)\,\mathrm{d}r_s = 20\pi k_l (T_{l2} - T_{l3}) Q_1 \quad (9)$$

where surface-area-averaged liquid temperature T_{l2} and volume-averaged liquid temperature T_{l3} are defined from the equations

$$T_{l2} Q_1 = \int_0^\infty T_s r_s n(r_s)\,\mathrm{d}r_s \quad \text{and} \quad T_{l3} Q_1 = \int_0^\infty \overline{T}_d r_s n(r_s)\,\mathrm{d}r_s \quad (10)$$

The latter is taken here to be the volume-averaged temperature evaluated from the liquid energy E_l obtained from Eq. (3).

Thus the liquid surface-average temperature is expressed as

$$T_{l2} = T_{l3} + \frac{\dot{Q}_{\text{in}}}{20\pi k_l Q_1} \quad (11)$$

Hence once T_{l3} and Q_1 are obtained from transport equations, T_{l2} can be evaluated, as long as $\dot{Q}_{\text{in}}$ can be found. The latter is done by evaluating the heat transfer by convection from the surrounding gas.

The use of simple correlations to obtain the convective heat transfer to/from a drop has been criticised, e.g. by Aggarwal et al. (1984), mainly because they are developed from experimental data taken under quasi-steady conditions. However, these correlations are used extensively in CFD simulations, again because of the difficulties associated with the implementation of more rigorous but complex models.

The particular model adopted here is that due to Faeth (1983) in which the convective heat transfer for a single drop is given by

$$\dot{Q}_{\text{c,d}} = 2\pi r_s k_g (T_g - T_s) Nu_d \frac{\ln(1+B_M)^{1/Le}}{(1+B_M)^{1/Le} - 1} \quad (12)$$

where Nu_d is the drop Nusselt number and Le, the Lewis number, is defined by $Le = Sc/Pr$, the ratio of the energy to mass diffusivities in the gas film around the drop, where Sc and Pr are the Schmidt and Prandtl numbers, respectively.

B_M is the mass transfer number, Spalding (1953), defined in terms of vapour mass fractions f by

$$B_M = \frac{f_s - f}{1 - f_s} = \frac{p_{v,s} M_v}{p_{a,s} M_a}(1 - f) - f \quad (13)$$

Here M denotes molecular weight or molar mass, subscripts 'a' and 'v' denote air and vapour, respectively while 's' denotes drop surface conditions, and non-subscripted values denote conditions in the surrounding gas.

The form of the Nusselt number correlation suggested by Faeth is rather complex for use within the current model. This is because of the need to integrate the convective heat transfer over the drop size range locally, as illustrated below. Thus, for this first derivation of the new model, a simpler form of correlation is adopted, due to Ranz and Marshall (1952)

$$Nu_d = 2 + 0.6 Re_d^{0.5} Pr^{0.333} \quad (14)$$

where Re_d is the Reynolds number, defined by

$$Re_d = \frac{2\rho_g (U_d - U_g) r_s}{\mu_g} \quad (15)$$

and the Prandtl number is independent of drop size.

The convective heat transfer rate must be equal to that entering the drop, therefore $\dot{Q}_{\text{in,d}} = \dot{Q}_{\text{c,d}}$. Thus integration of Eq. (12), incorporating Eq. (14), over all drops locally results in

$$\begin{aligned}\dot{Q}_{\text{in}} &= 2\pi k_g \int_0^\infty (T_g - T_s) \frac{\ln(1+B_M)^{1/Le}}{(1+B_M)^{1/Le} - 1} \times \left(2r_s + 0.6\left(\frac{\rho_g (U_d - U_g)}{\mu_g}\right)^{0.5} Pr^{0.333} r_s^{1.5}\right) n(r_s)\,\mathrm{d}r_s \\ &= 2\pi k_g \frac{\ln(1+B_M)^{1/Le}}{(1+B_M)^{1/Le} - 1} \times (T_g - T_{l2}) \left[2Q_1 + 0.6\left(\frac{\rho_g (U_{l2} - U_g)}{\mu_g}\right)^{0.5} Pr^{0.333} (Q_2 Q_1)^{0.5}\right] \\ &= 2\pi k_g \frac{\ln(1+B_M)^{1/Le}}{(1+B_M)^{1/Le} - 1} (T_g - T_{l2}) Q_1 Nu_Q \end{aligned} \quad (16)$$

Here the surface-area-averaged velocity U_{l2} has been adopted in the Reynolds number as the most appropriate mean liquid velocity, and non-integer moments are approximated by appropriately weighted powers of the surrounding moments. Nu_Q and Re_Q are Nusselt and Reynolds numbers newly-defined in this work to apply to the whole of the spray locally

$$Nu_Q = 2 + 0.6 Re_Q^{0.5} Pr^{0.333}, \quad Re_Q = \frac{2\rho_g (U_{l2} - U_g)}{\mu_g}\left(\frac{Q_2}{Q_1}\right)^{0.5} \quad (17)$$

Some of the energy that enters the drops is lost back to the gas due to evaporation. The evaporation rate is expressed through the drop Sherwood number Sh_d

$$\dot{m}_d = 2\pi r_s \rho_g D_g Sh_d \ln(1 + B_M) \quad (18)$$

where D_g is the mass diffusivity. Again the correlation due to Ranz and Marshall has been employed:

$$Sh_d = 2 + 0.6 Re_d^{0.5} Sc^{0.333} \quad (19)$$

Using this correlation, the mass transfer source term for the spray locally is given from Eq. (18), after integration across all the drops, by

$$S_m = 2\pi \rho_g D_g \ln(1 + B_M) Q_1 Sh_Q \quad (20)$$

where

$$Sh_Q = 2 + 0.6Re_Q^{0.5}Sc^{0.333} \tag{21}$$

Following the method of Beck and Watkins (2003b), the equivalent source term, due to mass evaporation, for the surface-area moment S_{Q2} is given by

$$S_{Q2} = \rho_g D_g \ln(1 + B_M) Q_0 Sh_{Q0} \tag{22}$$

where

$$Sh_{Q0} = 2 + 0.6Re_{Q0}^{0.5}Sc^{0.333} \tag{23}$$

$$Re_{Q0} = \frac{2\rho_g(U_{l2} - U_g)}{\mu_g}\left(\frac{Q_1}{Q_0}\right)^{0.5} \tag{24}$$

The liquid energy equation source term $S_E = -\dot{Q}_{in}$ is the difference between the heat arriving at the drop surface through convective heat transfer and that lost due to evaporation of part of the liquid, i.e.

$$S_E = -2\pi Q_1\left[k_g\frac{\ln(1+B_M)^{1/Le}}{(1+B_M)^{1/Le}-1} \times (T_g - T_{l2})Nu_Q - \rho_g D_g \ln(1+B_M)LSh_Q\right] \tag{25}$$

where L is the latent heat of evaporation.

After substitution of Eq. (25) into Eq. (11) and rearrangement, there results

$$T_{l2} = \frac{T_{l3} + \alpha T_g + \beta}{1+\alpha}$$
$$\alpha = \frac{0.1k_g}{k_l}\frac{\ln(1+B_M)^{1/Le}}{(1+B_M)^{1/Le}-1}Nu_Q, \quad \beta = -\frac{0.1\rho_g D_g}{k_l}\ln(1+B_M)LSh_Q \tag{26}$$

In the above heat and mass transfer equations, the gas properties are evaluated using correlations involving the film mean temperature T_m. The one-third rule is applied to the spray locally as a whole, so that

$$T_m = \frac{(2T_{l2} + T_g)}{3} \tag{27}$$

The correlations used for the air properties and the liquid and vapour properties for the three fuels examined in this work are taken from Perry and Green (1997) and Timmermans (1965).

2.5. Drop break-up and collision models

Drop break-up plays a significant role in determining the level of heat and mass transfer to/from small drops, as is illustrated later in the results section of this paper. For that reason information about the relevant models of drop break-up and drop collisions are included here for clarity. These have been presented before by Beck and Watkins (2002), so only a précis of the methods and the final equations are included.

The break-up model accounts for the effects on the drop distribution function moments of unstable drops undergoing bag or stripping break-up. The thresholds determining these two events, developed by Nicholls (1972), have been used in many Discrete Droplet Model codes and have been adapted for the current model. In order to break-up, not only are the drops required to reach these unstable thresholds, but also require sufficient time. The break-up times determined by Nicholls are also used here. The break-up criteria are rearranged to give critical radii above which the drops are unstable, by assuming that the drops which are large enough to break are travelling at approximately the local mass-average velocity. Using these critical radii the number of drops potentially undergoing each type of break-up can be approximated by use of the drop size distribution. The proportion of these drops actually breaking up within a time step is given by the ratio of the time step and the time taken for an unstable drop to break-up.

The correlation of Faeth et al. (1995) for the Sauter Mean Radius (SMR) of sibling drops after stripping break-up is used to determine the change in surface area due to the break-up of a single drop. The change in the surface area per unit time for a single drop is obtained by dividing by the appropriate residence time for an unstable drop. This expression is then averaged over the drops undergoing break-up, using the number size distribution, to obtain the final equation for the source term component due to stripping break-up in the transport equation for the surface-area-averaged moment of the number size distribution

$$S_{Q_2,s} = \frac{(Q_{2,s}Q_{1,s})^{\frac{1}{2}}}{6.2\left(\frac{\rho_l}{\rho_g}\right)^{\frac{1}{4}}\left(\frac{\mu_l}{2\rho_l U_{rel}}\right)^{\frac{1}{2}}\frac{C_s}{U_{rel}}\left(\frac{\rho_l}{\rho_g}\right)^{\frac{1}{2}}} - \frac{Q_{1,s}}{\frac{C_s}{U_{rel}}\left(\frac{\rho_l}{\rho_g}\right)^{\frac{1}{2}}}, \tag{28}$$

where $Q_{1,s}$ and $Q_{2,s}$ are the sum of radii and total sum of squares of radii of the drops undergoing stripping break-up and U_{rel} is the difference between the mass-averaged liquid velocity and the gas velocity. For the calculations presented to-date $C_s = 1.0$ has been used and found to give good predictions of experimental data on drop sizes. There is no source term for the Q_3 moment equation due to break-up as the total volume of drops is unchanged.

For bag break-up, no appropriate correlation on sibling sizes has been found in the literature, and so the surface area is assumed to double in the break-up, which is equivalent to the production of eight equally sized drops. This is again expressed as a change in surface area. Application of the number size distribution and integration over those drops breaking up in this regime leads to the component of the source term due to bag break-up as

$$S_{Q_2,b} = \frac{(Q_{0,b}Q_{1,b})^{\frac{1}{2}}}{\pi\left(\frac{\rho_l}{2\sigma}\right)^{\frac{1}{2}}}. \tag{29}$$

$Q_{1,b}$ and $Q_{0,b}$ represent the sum of radii and number of the drops undergoing bag break-up.

These two contributions to the change in the surface-area drop size distribution moment are then summed to give the total change in the surface-area-averaged moment

equation source term due to break-up. The combined term is also denoted as B_{Q2} in Table 1 for surface-area averaged momentum conservation.

The collisions model is semi-empirical, and has three stages. The first stage is to determine the number of collisions between drops occurring in any control volume. This is based on the collision frequency concept of O'Rourke and Bracco (1980). Their expression for the probability of a collision between two drops per unit volume per unit time, providing they are in the same control volume, is adapted to the new model by multiplying this collision probability by the appropriate number distributions and integrating over all drops. The relative velocity between drops U_{rel} is approximated by assuming a mean relative value between all colliding drops. With this assumption

$$N_{coll} = C_{coll}\pi U_{rel}(Q_0 Q_2 + Q_1^2), \tag{30}$$

C_{coll} is a model constant whose value has been found to be 0.15 by Beck and Watkins (2002) by comparison of model results with experimental data on drop sizes. The relative velocity U_{rel} between drops is approximated by assuming that the large drops are travelling at approximately the mass-average velocity, and the small drops have been fully entrained to the gas velocity. Thus the average drop–drop relative velocity is approximated as one half of the relative velocity between the mass-average liquid velocity and the local gas velocity.

The second stage of the model determines how many of these collisions result in each of the regimes of coalescence, bounce and separation, described by Orme (1997). The two parameters required to determine these proportions are the Weber number We and the impact parameter, b. The latter is defined as the perpendicular distance from the centre of one drop to the relative velocity vector placed on the centre of the other drop at impact, normalised by the sum of the radii. Charts of the different collision regimes as functions of We and b have been published by Jiang et al. (1992) and are used to provide the probabilities of each of the possible outcomes. The critical Weber numbers shown on the charts are translated into critical radii and the number size distribution is used to determine the probability that any given drop lies between adjacent critical radii. The outcome of a collision is decided by the Weber number of the smaller drop, according to Orme, and the impact parameter. For hydrocarbon drops, as addressed in this paper, there exist three critical radii, r_a, r_b and r_c, based on the three critical values of $We_a = 2.5$, $We_b = 10$ and $We_c = 30$. Again U_{rel} is used in this analysis. Probabilities for drop coalescence and drop separation are calculated. Collisions occurring in the bounce regime can be ignored in this model because the total mass, surface area and momentum of the liquid are conserved during a bounce collision, and hence there is no net change to any of the spray parameters considered in the model.

Modelling the impact parameter as a uniform random variable on $[0,1]$, as all values are equally likely, determines what proportion of the collisions occurring with the smaller drop between given critical radii result in each collision regime. These values are given in Table 2. Hence the total coalescence probability for hydrocarbon drops is given by

Table 2
Probabilities of collision outcome for hydrocarbon drops given radius of smaller drop

	P_{coll}	P_{sep}
$r_{smaller} < r_a$	0.6	0
$r_b < r_{smaller} < r_c$	0.5	0
$r_{smaller} > r_c$	0.2	0.8

$$P_{coal} = P_{coal,a} + P_{coal,b} + P_{coal,c} \tag{31}$$

where

$$P_{coal,a} = 0.6P(r < r_a)(2 - P(r < r_a)) \tag{32a}$$

$$P_{coal,b} = 0.5P(r_b < r < r_c)(P(r_b < r < r_c) + 2P(r > r_c)) \tag{32b}$$

$$P_{coal,c} = 0.2P(r > r_c)^2 \tag{32c}$$

are the probabilities of a collision with the smaller drop between each set of critical radii. The probability of separation is

$$P_{sep} = 0.8P(r > r_c)^2. \tag{33}$$

The final stage of the collisions model is to determine the effect of the predicted collisions on the drop surface area moment of the size distribution, as the liquid volume is conserved during collisions. The surface area change is approximated by that obtained from a collision between two drops of equal radius and to result in either one (coalescence) or five (separation) drops, also of equal radius, such that the total drop volume is conserved. The radius of the drops entering the collision, r_{in}, is dependent on the Weber number, and the value it takes for each regime is presented in Table 3 for hydrocarbon drops, along with the change in the square of the radius, δQ_2, resulting from the collision.

Hence the final source term due to collision of drops for the surface area moment is

$$S_{Q_2,coll} = N_{coll}(P_{coal,a}\delta Q_{2,a} + P_{coal,b}\delta Q_{2,b} + P_{coal,c}\delta Q_{2,c} + P_{sep}\delta Q_{2,sep}) \tag{34}$$

Table 3
Determination of surface area change for collisions between hydrocarbon drops

	Initial drop size, r_{in}	Change in square of radius
$r_{smaller} < r_a$	r_a	$\delta Q_{2,a} = (2^{2/3} - 2)r_{in}^2 = -0.41r_{in}^2$
$r_b < r_{smaller} < r_c$	$0.5^*(r_b + r_c)$	$\delta Q_{2,b} = (2^{2/3} - 2)r_{in}^2 = -0.41r_{in}^2$
$r_{smaller} > r_c$ (coalescence)	r_c	$\delta Q_{2,c} = (2^{2/3} - 2)r_{in}^2 = -0.41r_{in}^2$
$r_{smaller} > r_c$ (separation)	r_c	$\delta Q_{2,sep} = (5.(0.4)^{2/3} - 2)r_{in}^2 = 0.71r_{in}^2$

2.6. Gas phase transport equations

All of the gas phase transport equation can be written in the general form

$$\frac{\partial}{\partial t}(\rho_g \theta \varphi) + \frac{\partial}{\partial x_k}(\rho_g \theta U_{gk} \varphi) = \frac{\partial}{\partial x_k}\left(\Gamma_\varphi \theta \frac{\partial \varphi}{\partial x_k}\right) + \theta S_\varphi + S_\varphi^l \tag{35}$$

The void fraction θ is defined by

$$\theta = 1 - \frac{4\pi Q_3}{3} \tag{36}$$

The particular forms of Γ_φ, S_φ and S_φ^l are given in Table 4 for values of φ representing continuity (1), momentum (U_{gj}), energy (E_g), vapour mass fraction (f), turbulence kinetic energy (k) and its dissipation rate (ε).

The presence of vapour changes the properties of the carrier gas. The state equation becomes

$$p = \rho_g R_0 \left(\frac{1-f}{M_a} + \frac{f}{M_v}\right) T_g \tag{37}$$

where R_0 is the universal gas constant. The specific heat capacity of the gas mixture is given by

$$c_{p,g} = \frac{(1-p_r)M_a c_{p,a} + p_r M_v c_{p,v}}{(1-p_r)M_a + p_r M_v} \tag{38}$$

where the ratio of the partial pressure of the vapour, averaged between the local spray surface value $p_{v,s}$ and the far field value, to the total pressure p, is given by

$$p_r = \frac{(p_{v,s} + \frac{R_0 p f}{R_g M_v})}{2p}. \tag{39}$$

where R_g is the mixture gas constant.

2.7. Solution scheme

The spray test cases studied in this paper are axisymmetric, thus here all the conservation or transport equations for both the liquid and gas phases are solved on the same two-dimensional (z,r) axisymmetric orthogonal computational grid. A staggered grid arrangement is adopted for the liquid and gas phase velocity components. Euler implicit temporal differencing and hybrid upwind/central spatial differencing are employed to render all the liquid and gas phase transport equations into finite volume forms. Discussion of these processes and the algorithm used can be found in Beck and Watkins (2002). For clarity the major algorithm steps are reproduced here.

The solution algorithm is based on the PISO algorithm of Issa (1986), with the liquid phase equations added into it. The PISO algorithm provides an efficient non-iterative solution procedure that couples the gas-phase pressure and velocity components by an operator splitting technique and solves the equations of motion for the gas phase in a predictor–corrector fashion. The current scheme solves the liquid equations only once, at the beginning of the time step. The use of a non-iterative scheme implies that some effects are lagged, i.e. carried forward from one time step into the next. In the current approach, the drop break-up and collision effects are calculated at the end of the time step, and the amended source terms for the Q_2 equations and for the surface-area averaged momentum equations are therefore carried forward to the beginning of the next time step.

The solution proceeds in the following manner at each time step:

Step 1. The transport equations for the moments Q_2 and Q_3 of the drop size distribution and for the liquid energy E_l, are solved. The void fraction is updated. Moments Q_0 and Q_1, requiring approximation from the assumed distribution, are calculated, as are T_{l3} and T_{l2}.

Step 2. The inter-phase drag source terms are evaluated.

Step 3. The transport equations for the moment-average liquid velocities U_{l2} and U_{l3}, are solved.

Step 4. The gas phase velocity components are predicted using the gas phase momentum equations.

Table 4
Forms of Γ_φ, S_φ and S_φ^l for gas phase equations

φ	Γ_φ	S_φ	S_φ^l
1	0	0	S_m
U_{gj}	μ_{eff}	$-\frac{\partial p}{\partial x_j} + \frac{\partial}{\partial x_k}\left(\mu_{\text{eff}}\left(\frac{\partial U_{gj}}{\partial x_k} + \frac{\partial U_{gk}}{\partial x_j}\right)\right) - \frac{2}{3}\frac{\partial}{\partial x_k}(\mu_{\text{eff}} \nabla \cdot \vec{U} + \rho_g k \delta_{jk})$	$S_m(U_{l3j} - U_{gj}) + S_{Ul3j}$
E_g	$\frac{\mu_{\text{eff}}}{\sigma_E}$	$\frac{\partial}{\partial x_k}(pU_{gk})$	S_E
f	μ_{eff}	0	S_m
k	$\frac{\mu_{\text{eff}}}{\sigma_k}$	$G - \rho_g \varepsilon$	0
ε	$\frac{\mu_{\text{eff}}}{\sigma_\varepsilon}$	$\frac{\varepsilon}{k}(c_{\varepsilon 1} G - c_{\varepsilon 2}\rho_g \varepsilon) + c_{\varepsilon 3}\rho_g \varepsilon \nabla \cdot \vec{U}$	0
$\mu_{\text{eff}} = \mu_{\text{lam}} + c_\mu \rho_g \frac{k^2}{\varepsilon}$			
$G = \rho_g c_\mu \frac{k^2}{\varepsilon}\left(\frac{\partial U_{gj}}{\partial x_k} + \frac{\partial U_{gk}}{\partial x_j}\right)\frac{\partial U_{gj}}{\partial x_k}$			
Prandtl numbers		Turbulence model constants	
σ_E	0.9	c_μ	0.09
σ_k	1.0	$c_{\varepsilon 1}$	1.44
σ_ε	1.3	$c_{\varepsilon 2}$	1.92
		$c_{\varepsilon 3}$	−0.373

Step 5. The first set of pressure correction equations are solved (see Issa, 1986 for details), as are the gas phase transport equations for energy E_g and vapour mass fraction f. The gas phase pressures, densities and velocity components are corrected.

Step 6. The second set of pressure correction equations is solved. The gas phase pressures, densities and velocity components are corrected again.

Step 7. Transport equations are solved for the turbulence kinetic energy and its dissipation rate. The equations are coupled and iterated to convergence. The turbulent viscosity is recalculated.

Step 8. Source terms are calculated for the effects of the break-up of unstable drops and collisions between drops on the Q_2 transport equations and on the surface-area averaged momentum equations.

The stability and robustness of this scheme has been demonstrated by the ability of the method to obtain converged solutions of the equations for all the test cases that have been attempted to date. The accuracy of the method has been partially assessed in earlier publications, and is further assessed in the following section of this paper, by comparisons with experimental data on spray penetration and drop sizes for a number of test cases.

Numerous grid and time-step dependence tests have been carried out in the earlier publications. The results from those tests have been used to set these parameters in this work, so that the results presented here are grid and time-step independent.

3. Test cases

3.1. Introduction

A number of test cases are employed to assess the accuracy of the predicted behaviour of the heat transfer, evaporation and transport processes. These cases are used to explore modelling and numerical aspects of the research. Experimental results reported by Levy et al. (1997) and Naber and Siebers (1996) allow some limited comparisons for diesel fuel cases that cover a wide range of gas temperature conditions. Some of these cases were also used for comparison purposes by Beck and Watkins (2004). Some parametric explorations are reported, concentrating on the effects of the fuels used and on the assumed mean drop sizes at inlet.

3.2. Levy et al. (1997) test cases

3.2.1. Introduction

Simulations are made using three fuels, *n*-dodecane, *n*-octane and *n*-heptane, based on the test conditions of Levy et al. These tests are designed to check that the model captures all necessary effects regarding the heat transfer and evaporation models. Therefore, these tests are carried out for different initial gas phase temperatures within the range of the liquid injection temperature of 293 K to the respective saturation temperature of each fuel, which at 2 MPa are 658 K, 560 K and 540 K for *n*-dodecane, *n*-octane and *n*-heptane, respectively. The assumed SMR of the spray at inlet is also investigated to assess the effect of the range of drop sizes employed on the surface-area-averaged temperatures and volume-averaged temperatures. The conditions used are summarised in Table 5.

Data relating to the injection of fuel into the cylindrical chamber, and also some relevant geometrical parameters are given in Table 6. To provide inlet conditions the nozzle exit is divided radially into the upstream faces of two cells. Then mass and momentum conservation equations are solved across these two cells to obtain liquid and gas phase velocity components, and the void fraction. The void fraction provides the inlet value of Q_3. The assumed SMR allows the inlet value of Q_2 to be evaluated. More details of the equations solved are given in Beck and Watkins (2002). Calculations are run with the 109×73 line grid shown in Fig. 1 with the grid clustered around the nozzle exit at the top left hand edge of the grid, so that the minimum grid spacing in the axial direction is 0.5 mm, and the two injector cells fitted within the expansion of the spray over this distance. The simulations are run using a time step of 1 μs within a total time of the simulation of 1.0 ms. Air is used as the ambient gas.

Table 6
Injection characteristics and geometrical parameters of the nozzle and the cylindrical chamber used for Levy et al. (1997) test cases

Quantity (Units)	Value
Nozzle opening pressure (MPa)	17
Ambient pressure (MPa)	2
Nozzle radius (mm)	0.10
Axial length of the chamber (mm)	100
Chamber radius (mm)	40

Table 5
Levy et al. (1997) test cases

Name	Gas temperature (K)	Gas density (kg/m^3)	Injection SMR (μm)	Heat and mass transfer equations
L1	443	15.73	7	12–26
L2	598	11.65	7	12–26
L2V	598	11.65	7	12–25 TL2 = TL3
L2-70BU	598	11.65	70 With break-up/collision models	12–26
L2-70NBU	598	11.65	70 No break-up/collision models	12–26

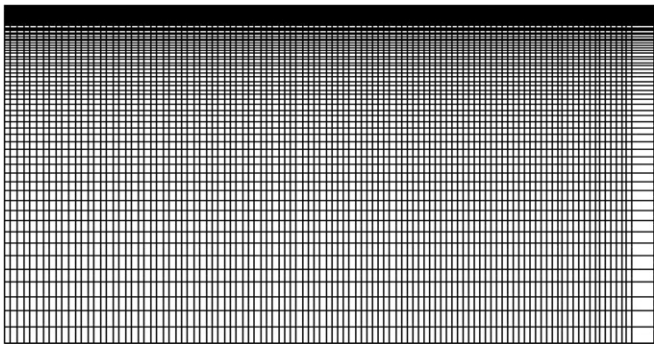

Fig. 1. Grid used for the Levy et al. (1997) test cases.

3.2.2. Comparisons with experimental data

Before considering the heat and mass transfer models in detail, the results of simulations using *n*-dodecane are compared with experimental data obtained by Levy et al. For these comparisons both of the liquid phase temperatures are calculated, as described in the model above. However, the data available are relatively insensitive to the temperature used in the heat and mass transfer models, although, as shown later these do have a large impact on certain aspects of the results.

In order to achieve as good an agreement as possible with the data, the inlet conditions were matched as closely as possible to the data given by Levy et al. In particular, the variation of injection pressure with time was reproduced to an error of a few percent by dividing the injection period into two parts. In the first 0.15 ms the injection pressure rises linearly with time from an initial value of 17.73 MPa to its maximum value of 18.33 MPa. In the second period up to 1.0 ms the injection pressure drops linearly to 10.05 MPa. As a consequence the computed injection velocity follows similar trends. The measured spray angle was also used in order to set the temporal variation of the radial component of the liquid velocity at injection. A constant value of discharge coefficient was set at 0.62.

Fig. 2 shows the predicted variations of the liquid velocity components after 1.0 ms. The experimental data are taken over the first 1.0 ms, so includes some effects of the transience of the spray. The second moment velocity components are used for this comparison, as they are closer in nature than volume-averaged velocities to the number averaged velocity that would be evaluated in the experiments. However, the surface-area-averaged velocities are predicted to be only a few percent less than the volume-averaged velocities in these cases.

The sprays are predicted not to spread radially as far as the experiments indicate. This is particularly so for case L1. For this case the gas density is significantly higher than for case L2, due to the lower gas temperature, as shown in Table 5. One would expect that this confines the spray into

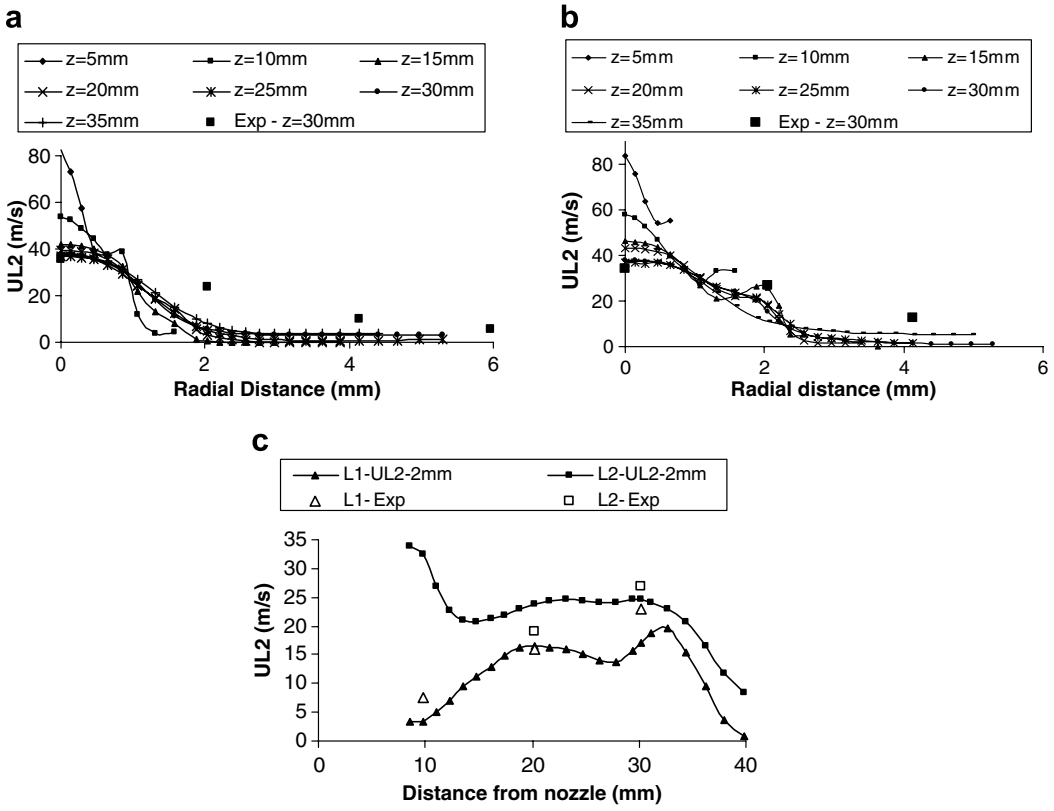

Fig. 2. Comparisons of predicted liquid velocity components with experimental data. (a) Radial variation of axial velocity – L1, (b) radial variation of axial velocity – L2 and (c) axial variation of axial velocity.

a narrower jet, as depicted by the calculations. The predictions show the fairly rapid diminution of the axial velocity component near the centreline of the spray, due to the large drag forces exerted on the drops here. By 30 mm downstream of the nozzle an essentially steady-state position for the axial velocity has been achieved here, in which the liquid and gas velocities are in equilibrium. The level of the liquid velocity is in good agreement with the experimental data. A reasonable agreement is found for case L2 out to about 2 mm from the centreline, before falling off more quickly than the experimental data suggests. Despite the relatively poor agreement with experiment for the radial variation of the axial velocity component for case L1, Fig. 2(c) shows that the axial variation matches closely with experiment. Data were taken at a radial position of 2 mm, and the predictions shown here mirror this. The liquid arrives at this radial position about 8 mm downstream of the nozzle. Thereafter both the level and variation of the velocity component agree well with the experimental data. The same can also be claimed for the case L2 results. The spray is predicted to arrive at the 2 mm radial position with a substantially higher axial velocity than for case L1. This is because of the faster spreading rate of the spray for case L2. However, no experimental data were given at the 10 mm position, so this observation cannot be checked. Further downstream the level and variation of the velocity are reasonably well predicted, although the level of agreement is not as good as for case L1.

Given the apparent under-prediction of the spreading of the sprays compared to the measured ones, it would be expected that the penetration of the sprays be over-predicted. However, as shown in Fig. 3, this is not the case. The way in which penetration is evaluated is always a problem in spray predictions, particularly when using discrete drops. A few 'rogue' drop parcels can distort the result if care is not taken. Here, because a continuum approach is used, such problems do not arise. Instead the liquid volume calculations can be used to determine where the front of the spray is, as shown in Fig. 3(a). This figure also illustrates the way in which the liquid is slowed by the ambient gas and forms into a head where a larger percentage of the liquid can be found. The slope of the liquid volume or concentration increases at the front of the spray as the drag forces are continuously imposed on the drops and the front of the spray decelerates more quickly with time. Plots like Fig. 3(a) have been made for all the test cases simulated in this paper. From these plots, the penetration can be evaluated as being the position, at any given time, where the liquid volume approaches the zero value at the head of the spray.

The results of this exercise are shown for cases L1 and L2 in Fig. 3(b). The variations of the predicted penetrations and those of the experiment are not identical. The latter shows a two stage variation, in both stages of which the penetration varies roughly linearly. The first stage lasts up to about 0.1 ms. In contrast the predictions vary more continuously. As a consequence there is over-prediction of the penetration from about 0.1 ms up to 0.5 ms, followed by under-prediction thereafter. However, the error is never more than 5–10%.

The final sets of experimental data are mean drop sizes, as shown in Fig. 4. These are obtained as average values across the spray at the indicated axial locations. These are also obtained over a finite time span, and therefore will include some effects of transience in the spray. The predicted values are also averaged over the spray, but are a snap-shot at 0.8 ms. To obtain these results the SMR at inlet is taken to be 7 μm. However, as shown below, the results are relatively insensitive to this assumption, as long as drop break-up and collision models are activated, as is done here. Both the experiment and the simulation indicate little variation in the SMR along the spray, except that the simulations predict a significant increase in mean drop sizes at the front of the spray, where the drops are closer together due to the slowing produced by the drag. This produces more drop collisions and hence larger drops. The agreement between the experimental data and the predictions is far from perfect, although everywhere the errors are less than 20%, except at the spray head for case L2.

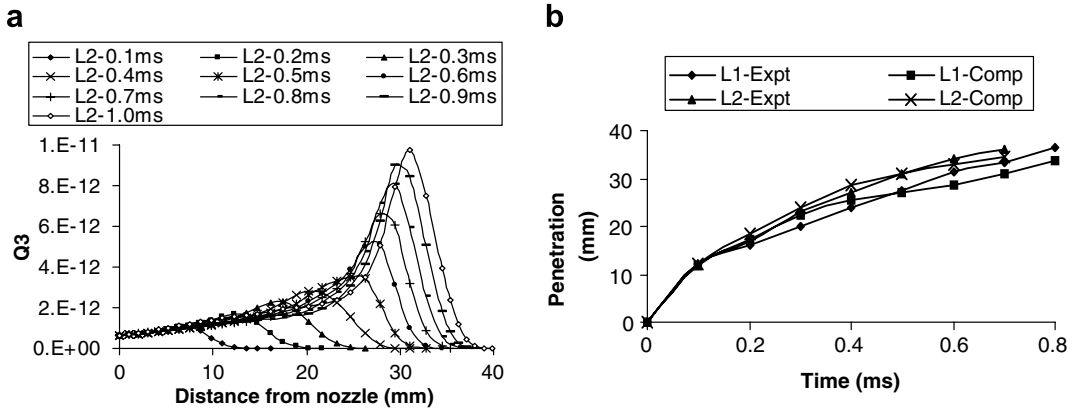

Fig. 3. Comparisons of predicted penetrations with experimental data. (a) Axial variation of liquid volume and (b) penetration.

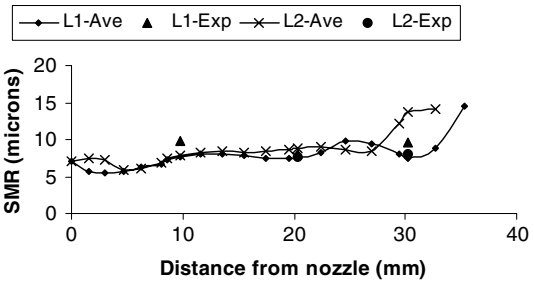

Fig. 4. Comparisons of predicted mean drop sizes with experimental data.

3.2.3. Predictions of temperatures and fuel vapour mass fractions

In this section the effects are assessed of using the second liquid temperature based on drop surface conditions. Unfortunately, there are no experimental data by which to judge the accuracy of these predictions.

Fig. 5(a) and (b) shows the predicted temperature variations along the spray centreline at 1.0 ms, for the two cases. In both cases there appears to be little difference between the volume-averaged liquid temperature, denoted in these figures by TL3, and the surface-area-averaged liquid temperature, denoted by TL2, except near the nozzle where the gas temperature, denoted by TG, is relatively high. Here maximum differences of about 20 K are seen for case L1 and 40 K for the higher gas temperature case L2. There are also some differences observed in the spray head, again where the gas temperature is relatively high. However, it must be realised that this is the essentially steady-state condition for the spray throughout most of its length. The spray drops have been exposed to the high gas temperatures for a significant time period and thus the drops have had time to equalise out in terms of the temperature variations within the drops. Equally, the gas temperature has dropped significantly from its initial condition, and so the temperature difference between the gas and liquid is substantially reduced. This implies that both heat and mass transfer reduce as the spray proceeds downstream. These features also contribute to the equalisation of the liquid temperatures.

Earlier in the spray lifetime the liquid temperature differences are much higher throughout the spray, as shown in Fig. 5(c). These larger differences contribute to large variations in the mass transfer rates, both within the length of the spray and during the time variation. Despite the larger differences in liquid temperatures seen in Fig. 5(c), these are still much less than those predicted by Dombrovsky and Sazhin (2003), who obtained maximum differences of about 100 K. However, their results were for a single drop of 20 μm radius, and were for a gas temperature of 880 K which is more than 280 K higher than used here. The use of a single drop also results in no diminution of the gas temperature, unlike the situation with a spray were heat transfer to the multiplicity of drops results in a substantial decrease in gas temperature, as illustrated in Fig. 5. Later test cases with higher gas temperatures, described in Section 3.3.3, show much greater differences (up to 150 K) between the liquid temperatures.

The predicted variations of vapour mass fraction along the spray centreline at 1.0 ms are illustrated in Fig. 6. Vapour is produced throughout the lifetime of the spray, and is convected downstream by the gas flow. Gas flow velocities are lower than liquid velocities throughout most of the spray, particularly near the nozzle. So the vapour shown here is both that just produced at the position in question plus that accumulated over time due to convection from upstream. This is why it is important to recognise the effects of mass transfer rates that vary both in position and time.

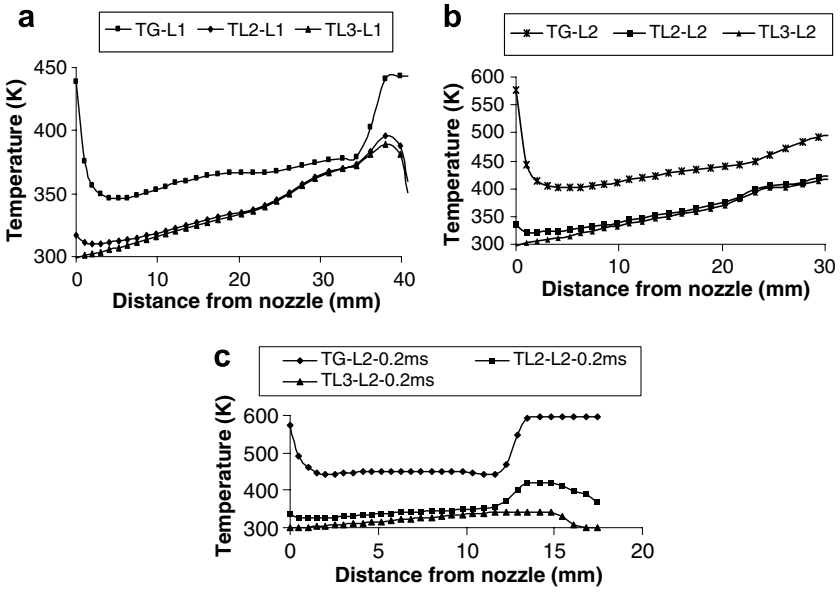

Fig. 5. Predicted centreline temperature variations. (a) Case L1, (b) case L2 and (c) case L2 at 0.2 ms.

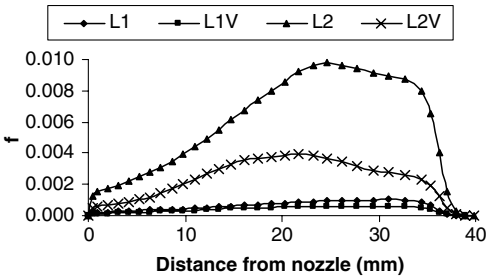

Fig. 6. Predicted centreline vapour mass fraction variations.

Fig. 6 shows the greatly increased vapour production from case L1 to case L2. The latter has a much higher ambient gas temperature, so that heat and mass transfer rates are substantially enhanced. Also shown in this figure are the effects of employing the volume-based liquid temperature TL3 in the equations for heat and mass transfer, instead of the surface-area based TL2. The curves based on TL3 are denoted by the letter V. With the scale of the diagram used here, the differences in vapour so produced do not appear large for case L1. However, in some parts of the spray near the head the mass of vapour produced by using temperature TL2 is at least 50% greater than those produced using TL3. For case L2, this effect is even greater. There is substantially more vapour produced near the nozzle where the gas temperatures are high and the differences between the two liquid temperatures are a maximum. These different levels of vapour are convected downstream and add to the greater production of vapour also occurring there, so that the maximum differences are seen near the spray head. Here the vapour levels predicted using TL2 are 4–5 times greater than those predicted using TL3.

The major reason for this large effect can be traced to the pressure of the vapour in the film around the drops. The mass transfer rates, as expressed through Eq. (18) is proportional to $\ln(1 + B_M)$, where B_M is the mass transfer number, given in Eq. (13). Eq. (13) shows B_M to be proportional to the pressure of vapour in the film. The vast majority of the gas surrounding the drops is composed of air so that the partial pressure of the air is much greater than that of the vapour. Consequently, values of B_M are much less than 1, and $\ln(1 + B_M)$ is proportional to B_M and hence the mass transfer rate is proportional to the pressure of fuel vapour. The equation for the pressure of vapour in the film is given by

$$p_{v,s} = e^{f(T_m)} \tag{40}$$

where for *n*-dodecane the function of the film temperature $f(T_m)$ is given by

$$f(T_m) = 137.47 - \frac{11976}{T_m} - 16.698\ln(T_m) + 8.0906 \times 10^{-6} T_m^2 \tag{41}$$

Consider the example where the gas temperature $T_g = 450$ K, and the surface-area-averaged temperature $T_{l2} = 350$ K. Employing the one-third rule Eq. (27), results in $p_{v,s} = 3235.1$ Pa. Now consider that $T_{l3} = 330$ K and this is used instead to calculate T_m and hence $p_{v,s}$, as was done for the calculations denoted by *V* in Fig. 6. Then $p_{v,s} = 1746.9$ Pa. Thus the mass transfer rate is nearly halved in this example. It has been shown above that the differences in T_{l2} and T_{l3} are higher than in this example during substantial parts of the spray development.

Whether or not such large differences between these two temperatures should be expected can be assessed by examining the Biot number of the spray locally. The Biot number expresses the balance between the heat transfer rate within the drops to the heat transfer rate due to convection at the drop surface. For a single drop this is expressed as

$$Bi_d = \frac{h r_s}{k_l} \tag{42}$$

where the convective heat transfer coefficient h is evaluated from the Nusselt number Nu_d, so that

$$Bi_d = \frac{k_g Nu_d}{k_l} \tag{43}$$

Following the integration method carried out above, the Biot number for the whole spray locally is then given by

$$Bi_Q = \frac{k_g Nu_Q}{k_l} \tag{44}$$

The predicted values of Bi_Q along the spray centreline at 1.0 ms are presented for the two cases in Fig. 7(a). These vary along the centreline but generally both lie within the range from 0.5 to 1.5. These will be minimum values for the spray, due to essentially steady-state conditions having been reached. Earlier in the spray development, higher levels can be expected. Even the values shown in Fig. 7(a) are well above the Biot number limit of 0.1 below which the

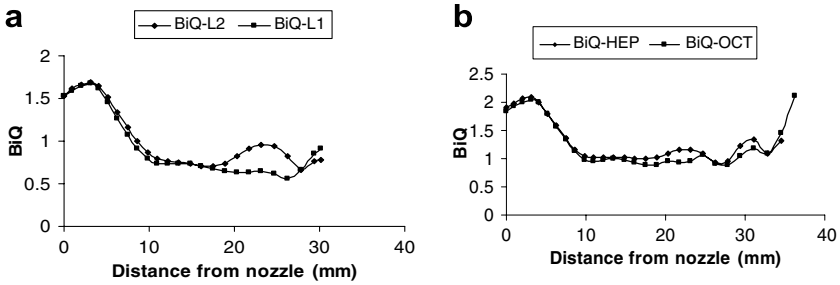

Fig. 7. Predicted centreline Biot number variations. (a) *n*-dodecane, (b) *n*-heptane and *n*-octane.

temperature variation within the drops can be neglected (Holman, 1992). The implication is that temperature variations across the drops must be expected. As an example, for a drop Biot number of 1.5, Holman shows that

$$T_s - T_g = 0.55(T_c - T_g) \tag{45}$$

where T_c is the centre point temperature of the drop. Employing Eq. (7), it is easy to show that

$$T_s = 0.247T_g + 0.753\overline{T}_d \tag{46}$$

Integrating using the number size distribution results in the equivalent equation

$$T_{l2} = 0.247T_g + 0.753T_{l3} \tag{47}$$

Taking the example of $T_g = 450$ K and $T_{l3} = 330$ K, results in $T_{l2} = 360$ K. Thus the results presented above agree well with this analysis.

Although not explicitly demonstrated here, the effects of using the surface-area-averaged temperatures in place of volume-averaged temperatures in the model of heat and mass transfer on macro scale features of the spray, such as penetration, are not significant. This is because, even if there is a substantial difference made in the evaporation of the liquid, the effects on drop sizes are still relatively insignificant. Thus it can be stated that earlier results obtained using this model in which volume-averaged temperatures were used are substantially correct, as long as the data used for comparison purposes related to phenomena such as penetration and mean drop sizes. This conclusion can also be extended to results produced by DDM-based computer codes. However, where the published results were extended to include the predictions of vapour mass fraction, then substantial errors in the results can be expected, as demonstrated in this paper.

Heat and mass transfer are surface related phenomena, therefore the results produced using surface temperatures must, in theory, be more accurate. Unfortunately, experimental data does not exist to demonstrate this. Whether the current model is accurate in all cases cannot therefore be properly assessed. As demonstrated by Dombrovsky and Sazhin (2003) the use of a parabolic temperature profile is likely to be least appropriate at entry of the drop into the hot gas. However, they also demonstrate that this effect is significantly reduced if the Biot number of the heat transfer is increased (to 5 in their case). This is similar to the situation in most of the cases discussed here, and would also apply to most examples of sprays injected using high pressure injectors into engine-like gas conditions.

3.2.4. Effects of the fuel used

In order to assess whether the model reacts properly to a change of fuel, the simulations above were repeated but with *n*-dodecane replaced by either *n*-heptane or *n*-octane. For both fuels the appropriate properties were inserted into the computer code. Two runs were made of the program in each case with the gas temperature set to either 400 K or 500 K. Otherwise the conditions are identical to those of the Levy et al. *n*-dodecane simulations just described.

The predicted centreline Bi_Q variations at 1.0 ms are presented for the two 500 K cases in Fig. 7(b). These variations are clearly very similar to the *n*-dodecane variations, indicating a similar effect of heat transfer on the liquid temperatures for all three fuels. There will be some differences in the actual heat transfer rates compared to the *n*-dodecane results because the gas temperature used for the cases presented in Fig. 7(b) is less (500 K compared to 598 K).

The actual mass transfer rates for both *n*-heptane and *n*-octane are much higher than for *n*-dodecane, despite the lower gas temperature. This is due to the greater volatility of these fuels, primarily expressed through the vapour pressure $p_{v,s}$ in the gas surrounding the drops. The equivalent equations to Eq. (41) for *n*-heptane and *n*-octane, respectively are

$$f(T_m) = 87.829 - \frac{6996.4}{T_m} - 9.8802\ln(T_m) + 7.2099 \times 10^{-6}T_m^2 \tag{48}$$

$$f(T_m) = 96.084 - \frac{7900.2}{T_m} - 11.003\ln(T_m) + 7.1802 \times 10^{-6}T_m^2 \tag{49}$$

For the same temperature conditions as in the example above for *n*-dodecane (using T_{l2}), Eq. (40) gives values for $p_{v,s}$ of 141,360 Pa for *n*-heptane and 64,660 Pa for *n*-octane. These pressures are many times higher than the corresponding value for *n*-dodecane. The resulting increased mass transfer rates lead to increased levels of vapour mass fraction in the surrounding gas, as depicted in Fig. 8. Here peak values of f for *n*-heptane and *n*-octane are about 4 and

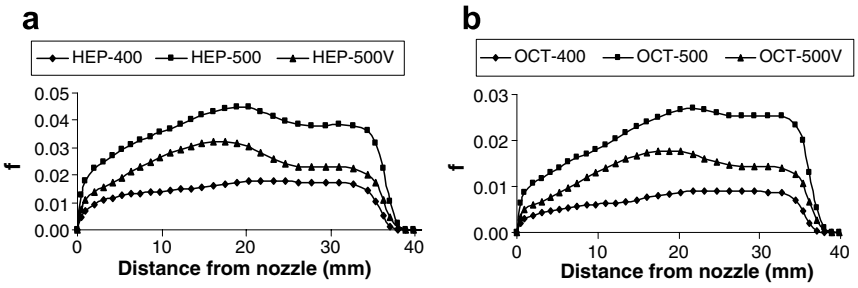

Fig. 8. Predicted centreline vapour mass fraction variations. (a) *n*-heptane and (b) *n*-octane.

2.5 times greater respectively than for *n*-dodecane. However, the levels are not as high as might be expected purely from the vapour pressure values. There are two reasons for this, apart from the distributive effects of convection and diffusion that are not easy to assess. As shown in Eq. (13) it is the product of the vapour pressure and the molecular weight or molar mass of the vapour that determines the level of f_s. The molar mass of *n*-heptane and *n*-octane are 110.20 kg/kmol and 114.22 kg/kmol, respectively, compared to 170.34 kg/kmol for *n*-dodecane. The second effect is due to the presence of the surrounding vapour mass fraction f in Eq. (13). For single drop analyses, this value is set to zero, because there is no vapour at a short distance away from the drop. This practice is often also followed in spray calculation schemes. However, if substantial amounts of vapour exist in the vicinity of the drops then the driving potential for mass diffusion of the vapour is diminished and less liquid can evaporate. This happens for the cases discussed here. For the values of f as shown in Fig. 8, these approach the same order of magnitude as f_s. Further simulations have been run without the presence of f in Eq. (13), the results of which show that the vapour mass fraction levels increase by some 20–30%.

3.2.5. Effects of drop sizes

As indicated in Table 5, to assess the effects of the drop sizes in the spray on heat and mass transfer rates, two further calculations were made using *n*-dodecane, as experimental data on mean drop sizes exist for this fuel. In the first simulation the assumed SMR at inlet was raised from 7 μm to 70 μm, but the break-up and collision models were left activated. The resulting effects on the mean drop sizes and mass transfer are summarised in Fig. 9. Differences in drop sizes from the previous calculations are significant only over the first 10–15 mm from the nozzle. Perhaps unexpectedly, this results in a significant increase in the production of vapour near the nozzle, as shown in Fig. 9(b). The reason for this can be seen in Fig. 9(d), which shows the predicted Biot numbers. The presence of larger drops near the nozzle with high velocities relative to the gas phase results in enhanced levels of Reynolds numbers and hence Nusselt numbers in Eq. (17). The higher Biot numbers lead to greater differences between the liquid phase temperatures which in turn result in higher film temperatures and hence mass transfer rates. The larger drops near the nozzle also have the effect of dispersing the spray away from the centreline in this region; as a consequence the spray near the centreline becomes dilute more quickly downstream, leading to the earlier fall off of the vapour mass fraction here.

In the second new simulation the inlet SMR is left at 70 μm but the break-up and collision models are de-activated. As a consequence, the mean drop sizes in the spray remain at about 70 μm throughout the spray (not shown in Fig. 9(a)), except in the head region where increases are observed, due to the accumulation of larger drops there. The effects on the mass transfer are significant, as shown in Fig. 9(b). In agreement with the previous case, the Biot number near the nozzle is enhanced, indeed, due to the drops staying large, this effect continues further downstream. However, because of the reduced drag on the drops, the dispersion of the liquid away from the centreline is also increased, resulting in a diminution of the overall mass transfer rates from the smaller number of drops there. The effects on the liquid and gas temperatures are also very significant, as illustrated in Fig. 9(c). The substantially increased Nusselt numbers lead to T_{l2} temperatures that are significantly greater than T_{l3} temperatures, as can be seen from Eq. (26). In fact, with the chosen drop sizes, the volume-averaged drop temperatures hardly rise from their initial value, whereas the surface-area-averaged temperatures are 100 K greater. There is also little effect

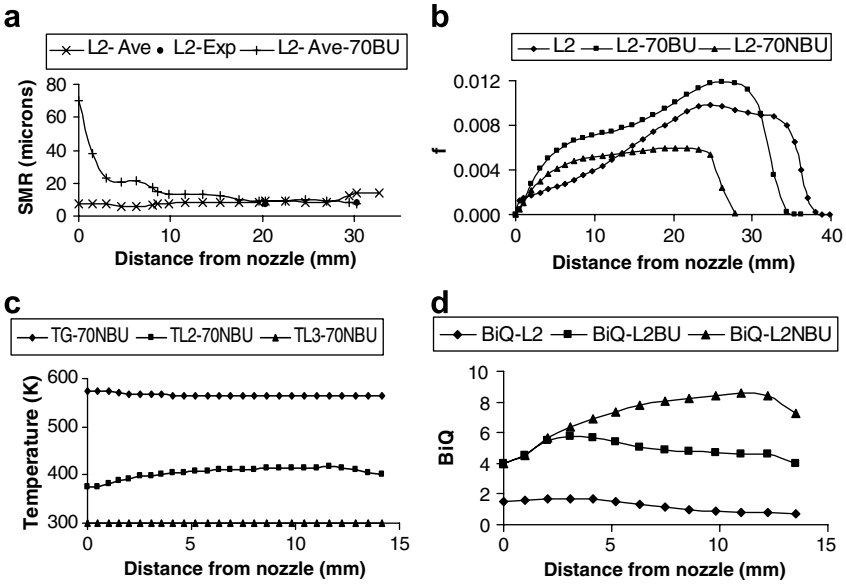

Fig. 9. Effects of initial drop sizes. (a) Mean drop sizes, (b) centreline vapour mass fraction, (c) centreline temperatures and (d) centreline Biot numbers.

on the gas-phase temperatures. This suggests that the increased heat transfer rate is being balanced by the mass transfer rate, as shown by Eq. (25), so that the net overall energy transfer between the phases is essentially zero. This is corroborated by the large amount of mass transfer, as previously discussed. This arises because the film temperature T_m is much larger for this case, resulting in significant levels of mass evaporation, for reasons discussed above, although not to the same level as for the smaller drop cases.

Dombrovsky and Sazhin (2003) did not make an explicit numerical investigation of the effects of drop size on the accuracy of the results obtained using the parabolic temperature model. However, the model was found to be least accurate in the early development of the temperature profile. The time over which inaccurate results were obtained depended on the Biot number Bi and the product of the Biot number and Fourier number $Fo = k_l t/(\rho_l c_{pl} r_d^2)$, where t is the elapsed time after injection. For a value of $Bi = 5$, similar to the values obtained in the cases shown here, the limiting value of $BiFo$ was found to be 0.10. The time scale over which the temperature profile develops is thus dependent on the square of the drop radius. For a 7 μm radius drop of hydrocarbon, the time scale is approximately 0.01 ms. For a 70 μm radius drop this would be 1 ms.

3.3. Naber and Siebers (1996) test cases

3.3.1. Introduction

The second set of experimental data used for assessment purposes in this paper is supplied by Naber and Siebers. As shown in Table 7, the conditions experienced by the sprays in these experiments are much more extreme than for the Levy et al. experiments. The injection pressure is high resulting in injection velocities that are more than three times greater than in the Levy et al. cases. The ambient gas temperature of 1000 K gives a gas to liquid temperature difference at inlet of more than 700 K, compared to a maximum of 300 K for the previous cases. Finally, the gas pressures and densities employed cover a much wider range of conditions. These test cases therefore present a difficult challenge to the capabilities of the model. Unfortunately the only independent data supplied by Naber and Siebers that can be used for comparison purposes are the penetration rates of the different sprays. The other experimental data supplied on injection rates and spray angles are used to set the injection conditions for the simulations. However, the comparisons with penetration data do allow an assessment of the capabilities of the model to accurately predict the hydrodynamics of the flow. In particular, the drag models are thereby assessed. Because of the stronger effects of heat and mass transfer in these cases, these are more likely to effect drop sizes and hence drop velocities. Therefore, these models are also assessed to some extent. All the simulations made in this section of the paper use the full heat and mass transfer model as detailed above, including the use of the surface-area-averaged temperature T_{l2} in the calculations, unless otherwise specified.

Table 7
Injection characteristics and geometrical parameters of the nozzle and the cylindrical chamber used for Naber and Siebers (1996) test cases

Name	NS1	NS2	NS3	NS4	NS5
Gas pressure (MPa)	0.94	1.94	3.99	8.21	16.83
Gas density (kg/m^3)	3.30	6.76	13.9	28.6	58.4
Gas temperature (K)	1000				
Nominal injection pressure difference (MPa)	137				
Nozzle radius (mm)	0.128				
Injection SMR (μm)	15				
Axial length of the chamber (mm)	120				
Chamber radius (mm)	40				
Simulation time step (μs)	0.5				
Simulation time (ms)	0.7	1.4	1.8	2.0	2.0

For these simulations a similar grid is used as for the Levy et al. test cases, as shown in Fig. 1. Differences arise because the grid is stretched in the axial direction to cover 120 mm, and the different nozzle diameter brings changes in the near orifice distributions in the radial direction, as explained in Section 3.2.1. To obtain time step independent results for these cases it was necessary to reduce the time step to 0.5 μs, i.e. half that used for the Levy et al. cases. This is because the increased injection velocities reduce the time scales of the flow.

3.3.2. Comparisons with experimental data

Penetration results for all five of the Naber and Siebers high gas temperature cases are shown in Fig. 10(a). Fig. 10(b) and (c) shows examples of the liquid volume axial distributions, as discussed in Section 3.2.2, from which the predicted penetration data are extracted. The distributions shown in Fig. 10(b) are, in particular, somewhat different from those shown in Fig. 3 for the Levy et al. cases. The effects of drag on the spray to re-distribute the liquid mass into the spray head does occur here, but to a much smaller extent. There is also a 'neck' apparent behind the spray head in which the liquid mass or volume is reduced below that both before it and after it in the spray. However, this change to the previously-seen distributions only occurs for the three higher gas density cases NS3, NS4 and NS5. The other two low density cases have Q3 distributions that are similar to those for the Levy et al. cases, as shown in Fig. 10(c). Thus this phenomenon is clearly associated with high levels of gas density and hence high levels of drag on the drops. However, the gas density in case NS3 has a value between those of the two Levy et al. cases, so this is not the only reason for this feature. These liquid volume results are obtained at the end of the simulations and the times used for the simulations vary, because the spray approaches the end of the calculation domain at different velocities in each case. The end times for the different simulations are shown in Table 7.

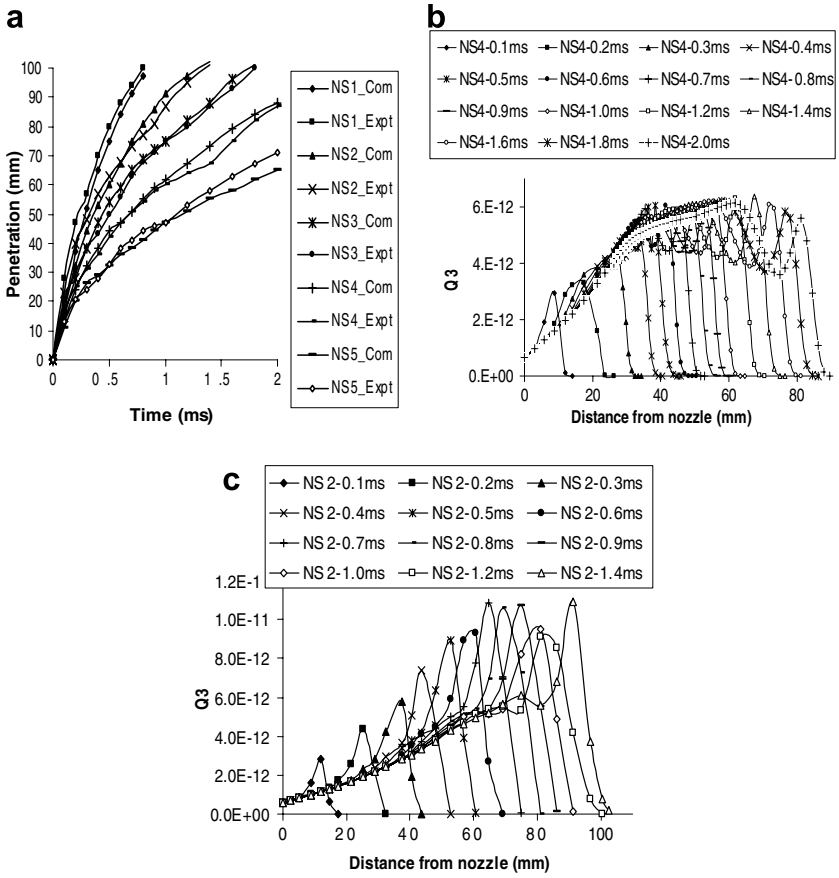

Fig. 10. Comparisons of predicted penetrations with Naber and Siebers (1996) experimental data. (a) Penetration, (b) liquid volume–high gas density and (c) liquid volume–low gas density.

Earlier results for the high density cases indicate that this 'necking' phenomenon only starts after about 0.5 ms, so it must be associated with the length of time that the drops in the front of the spray have been exposed to the very high gas temperatures, and hence to the amounts of heat and mass transfer that have occurred. It is certain that these drops will have evaporated more than later drops. More evidence of this is provided by Fig. 10(c). Although the general distribution has a similar shape to the Levy et al. cases, the proportion of the liquid in the head region is substantially lower in the Naber and Siebers cases. There is a slight change in the behaviour of the liquid volume in this case around 1.2 ms; this seems to be associated with the beginning of the 'necking' phenomenon.

The comparisons of predicted penetration rates with experimental data shown in Fig. 10(a) are generally very good. Percentage differences are less than 10 throughout for all the cases. There is some evidence that, in line with the Levy et al. test cases, the shapes of the penetration curves are not reproduced completely accurately, as, for example, in cases NS2, NS3 and NS5. However, it is clear that the model has reacted satisfactorily in terms of the gas density effects on the spray motion, and any effects associated with mass transfer on drop sizes and hence on fluid velocities have also been handled well.

3.3.3. Effects on temperatures and fuel vapour mass fractions

The effects of the high ambient gas temperature are manifested in a number of the gas phase properties, as depicted in Fig. 11(a) and (b). The vapour mass fraction centreline contours are presented at the end of the simulation time in each case. In all cases the predicted levels are several times higher than those shown in Fig. 6 for the Levy et al. cases. Here combustible levels of vapour/air mixing have been achieved. The lower gas density cases exhibit an almost uniform distribution, and the greater dispersion of the drops for these cases result in the dilution of the vapour in the centreline region relatively quickly downstream. The profile becomes more and more distorted with peak values towards the middle and front end regions as the gas density increases. There are thus present significant amounts of vapour at the head of these narrower sprays. This is a result of the increased vaporisation in the head of the spray due to the longer residence time for the latter cases. Despite this latter phenomenon the two liquid temperatures tend towards each other as the spray progresses downstream. In the near nozzle region the differences between these temperatures are very high, starting at about 250 K for case NS4, as shown in Fig. 11(b). Fig. 11(c) illustrates the Biot numbers in this region. Clearly the values returned by the predictions are much higher here than for the Levy et al. cases, for a similar size of injected drops,

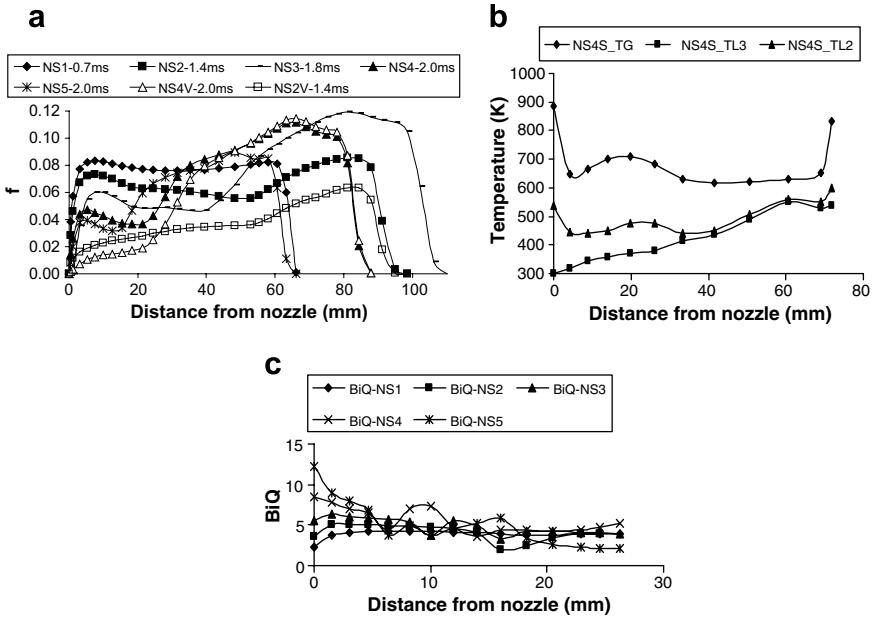

Fig. 11. Predicted centreline variations, Naber and Siebers test cases. (a) Vapour mass fractions, (b) temperatures and (c) Biot number.

implying the greater liquid temperature differences. The trend of the Biot number is downward as the distance from the nozzle increases, hence the convergence of the two liquid temperatures.

To determine the effects of using the surface-area-averaged temperatures in the heat and mass transfer equations for these very high gas temperature cases, two further simulations have been made, with the results shown in Fig. 11(a), denoted by the additional letter V. These employ the volume-averaged temperature in the heat and mass transfer equations. The predictions show that the low density cases (NS2 and NS2V) show similar trends to the Levy et al. cases in this respect, except that the effects are more prominent in the near-nozzle region, and become progressively less so as the spray proceeds downstream. This again emphasises the role of exposure time on mass transfer. This is seen to an even greater extent when the two high density cases (NS4 and NS4V) are compared. Differences are relatively large in the near-nozzle region, but these virtually disappear for much of the spray downstream.

4. Conclusions

This paper has described a variation on the approach to the modelling of sprays developed by Beck and Watkins (2003a). That model used a volume-averaged liquid temperature to determine heat and mass transfers between the phases. In practice it is the drop surface temperature that determines the heat and mass transfer rates. This paper has described the implementation of a simple model, within the overall moments approach to the modelling of sprays, which assumes a parabolic temperature profile within individual drops to calculate a surface-area-average temperature for the spray locally. This is believed to be the first instance of such a model being applied to spray simulations.

The model has been applied to the simulation of sprays having assumed drop size distributions with Sauter mean radii at inlet in the 7–70 μm range. Calculations have shown that surface-area-averaged temperatures and volume-averaged temperatures are substantially different over significant portions of the sprays, with greater differences found where the gas temperatures are highest. Calculations involving the Biot number have shown that these differences are to be expected.

The use of surface-area-averaged temperatures, in place of volume-averaged ones, results in substantially higher levels of mass being evaporated from the drops. This is predominantly because of the increased film mean temperature and resulting increases in the vapour pressure in the film. However, the role of exposure time to very high gas temperatures has to be taken into account.

The effects of the fuel used were also explored. The role of the vapour pressure in the film is again found to be the important parameter determining the different mass transfer rates for the different fuels.

Comparisons made with spray penetration data of diesel fuel for a wide range of injector and ambient gas conditions indicate that the model reacts correctly to changes in these parameters. Comparisons are also made with measured liquid velocities and mean drop sizes, with a reasonable level of overall agreement obtained with the measurements.

The importance of break-up and collision models on both the hydrodynamics and the heat and mass transfer, in simulations made with the larger drops at inlet, has been demonstrated.

Acknowledgements

The author wishes to thank his M. Phil. Research student Sergio Hernandez-Gonzalez for his help in partial development of the new heat and mass transfer model and for computer code development.

References

Abraham, J., 1997. What is adequate resolution in the numerical computations of transient jets? SAE Paper 970051.

Aggarwal, S.K., Tong, A.Y., Sirignano, W.A., 1984. A comparison of vaporization models in spray calculations. AIAA J. 22, 1448–1457.

Amsden, A.A., O'Rourke, P.J., Butler, T.D., 1989. KIVA-II: A computer program for chemically reactive flows with sprays. Technical Report LA-11560-MS, Los Alamos National Laboratory.

Beck, J.C., Watkins, A.P., 2002. On the development of spray sub-models based on droplet size moments. J. Comp. Phys. 182, 586–621.

Beck, J.C., Watkins, A.P., 2003a. On the development of a spray model based on drop-size moments. Proc. R. Soc. Lond. A 459, 1365–1394.

Beck, J.C., Watkins, A.P., 2003b. The droplet number moments approach to spray modelling: the development of heat and mass transfer sub-models. Int. J. Heat Fluid Flow 24, 242–259.

Beck, J.C., Watkins, A.P., 2003c. The simulation of water and other non-fuel sprays using a new spray model. Atomization Sprays 13, 1–26.

Beck, J.C., Watkins, A.P., 2004. The simulation of fuel sprays using the moments of the drop number size distribution. Int. J. Engine Res. 5, 1–21.

Chen, X.Q., Perreira, J.C.F., 1992. Numerical predictions of evaporating and non-evaporating sprays under non-reactive conditions. Atomisation Sprays 2, 427–433.

Crowe, C.T., Sharma, M.P., Stock, D.E., 1977. The particle-source-in-cell (PSI-CELL) method for gas-droplet flows. Trans. ASME J. Fluids Engrg. 99, 325–332.

Dombrovsky, L.A., Sazhin, S.S., 2003. A parabolic temperature profile model for heating of droplets, ASME. J. Heat Transfer 125, 535–537.

Ducowicz, J.K., 1980. A particle-fluid numerical model for liquid sprays. J. Comp. Phys. 35, 229–253.

Dunbar, C.A., Watkins, A.P., Miller, J.F., 1997. Theoretical investigation of the spray from a pressurized metered-dose inhaler. Atomization Sprays 7, 417–436.

Faeth, G.M., 1983. Evaporation and combustion of sprays. Prog. Energy Combust. Sci. 9, 1–76.

Faeth, G.M., Hsiang, L.P., Wu, P.K., 1995. Structure and break-up properties of sprays. Int. J. Multiphase Flow 21, 99.

Gosman, A.D., Johns, R.J.R., 1980. Computer analysis of fuel-air mixing in direct injection engines. SAE Paper 800091.

Holman, J.P., 1992. Heat Transfer, seventh ed. McGraw-Hill, London.

Issa, R.I., 1986. Solution of the implicitly discretised fluid flow equations by operator splitting. J. Comp. Phys. 61, 40.

Jahannama, M.R., Watkins, A.P., Yule, A.J., 2005. Electrostatic effects on agricultural air-atomised sprays and deposition: Part II: A computational study. Atomization Sprays 15, 629–660.

Jiang, Y.J., Umemura, A., Law, C.K., 1992. An experimental investigation on the collision behaviour of hydrocarbon droplets. J. Fluid Mech. 234, 171.

Levy, N., Amara, S., Champoussin, J.C., Guerrasi, N., 1997. Non-reactive diesel spray computations supported by PDA measurements. SAE Paper 970049.

Melville, W.K., Bray, K.N.C., 1979. A model of the two-phase turbulent jet. Int. J. Heat Mass Transfer 22, 647–656.

Mostafa, A.A., Elghobashi, S.E., 1985. A two-equation turbulence model for jet flows laden with vaporizing droplets. Int. J. Multiphase Flow 11, 515.

Mostafa, A.A., Mongia, H.C., 1987. On the modelling of turbulent evaporating sprays: Eulerian versus Lagrangian approach. Int. J. Heat Mass Transfer 30, 2583–2593.

Naber, J.D., Siebers, D.L., 1996. Effects of gas density and vaporization on penetration and dispersion of diesel sprays. SAE Paper 960034.

Nicholls, H., 1972. Stream and droplet break-up by shockwaves. NASA SP-194.

Orme, M., 1997. Experiments on drop collisions, bounce, coalescence and disruption. Prog. Energy Combust. Sci. 23, 65.

O'Rourke, P.J., Bracco, F.V., 1980. Modelling of drop interactions in thick sprays and comparison with experiment. In: Stratified Charge Auto Engines Conference, IMechE, London, p. 101.

Perry, R.H., Green, D.W., 1997. Perry's Chemical Engineers' Handbook, seventh ed. McGraw Hill.

Ranz, W.E., Marshall, W.P., 1952. Evaporation from drops. Chem. Eng. Prog. Part 1 48, 141–146.

Reitz, R.D., 1987. Modelling atomisation processes in high-pressure vaporising sprays. Atomisation Spray Tech. 3, 309.

Sirignano, W.A., 1999. Fluid Dynamics and Transport of Droplets and Sprays. Cambridge University Press.

Spalding, D.B., 1953. The combustion of liquid fuels. In: 4th Int. Symp. Comb.

Timmermans, J., 1965. Physico-Chemical Constants of Pure Organic Compounds, vol. 2. Elsevier Publishing Company.